Progress in Additive Manufacturing (2026) 11:2151–2163
https://doi.org/10.1007/s40964-025-01463-0

RESEARCH

In-Situ alloying of high-silicon soft magnetic alloy in laser powder bed fusion

Mümin Biyiklioglu[1] · Carolina Guerra[2] · Rossitza Setchi[1] · Philip Anderson[1]

Received: 27 June 2025 / Accepted: 28 November 2025 / Published online: 19 December 2025

Abstract
Additive manufacturing via laser powder bed fusion (LPBF) enables fabrication of complex high-silicon soft magnetic steels that are otherwise difficult to process. This study investigates the use of in-situ alloying of FeSi6.5 as a cost-effective alternative to pre-alloyed powder. As-built samples produced with commercial powder and as-blended samples using in-situ alloying were characterized for relative density, microstructure, and magnetic properties. The study showed that the commercial powder samples achieved higher densities (94.2–97.7%) than the as-blended samples (84.7–95.1%), while the as-blended specimens exhibited keyhole-type melt pools and finer, strongly<001>-textured grains. Saturation magnetizations of blended and commercial samples were comparable (up to ~1.88 T), while as-blended specimens consistently showed lower coercivity (1159–2 245 A/m) versus commercial counterparts (1468–2 414 A/m). Heat treatment at 1100 °C for 1 h reduced coercivity below 1000 A/m in all cases. Optimal magnetic-microstructural performance in as-blended samples was achieved at 90 µm pulse point distance and 150 µs exposure time, and at 90 µm pulse point distance and 100 µs exposure time for commercial powder. The results demonstrate that in-situ alloying produces FeSi6.5 components with competitive density, uniform Si distribution, favourable texture, and low coercivity after heat treatment, highlighting its potential for flexible, cost-effective LPBF of soft magnetic steels.

Keywords High-silicon soft magnetic steel · Laser powder bed fusion · In-situ alloying

1 Introduction

Additive manufacturing (AM), a family of production processes based on layer-by-layer material deposition, has undergone significant developments in recent decades. Since its inception with stereolithography in the 1980s, AM has expanded into various methods, including laser powder bed fusion (LPBF), directed energy deposition (DED), and fused deposition modelling (FDM) [1, 2]. Among these, LPBF has attracted particular interest for metal processing due to its high dimensional accuracy and low surface roughness [3]. Consequently, a wide range of alloys, especially steels, have been extensively studied using this method. Despite its advantages, LPBF is limited by its relatively low production rates compared to traditional manufacturing techniques [4].

One approach to enhance the efficiency and economic viability of LPBF is in-situ alloying, wherein elemental or partially pre-mixed powders are used instead of fully pre-alloyed powders. This strategy can reduce costs and enable flexible compositional tuning during the manufacturing process [5]. Numerous studies have explored in-situ alloying of Al and Ti with Si in LPBF manufacturing. Examples include the elemental blending of Al12Si and mixing pre-alloyed and elemental powder together in Al18Si alloys [6, 7], and Ti6Al4V(2–4)Fe in comparison to pre-alloyed powders [8]. In-situ alloying has also been applied to enhance manufacturability and improve mechanical properties, as

✉ Rossitza Setchi
setchi@cardiff.ac.uk

Mümin Biyiklioglu
BiyikliogluM@cardiff.ac.uk

Carolina Guerra
Carolina.guerra@nottingham.ac.uk

Philip Anderson
AndersonPI1@cardiff.ac.uk

[1] Cardiff School of Engineering, Cardiff University, Cardiff, UK

[2] Optics & Photonics Group, Faculty of Engineering, University of Nottingham, Nottingham, UK

seen in Si additions to Al7075 to mitigate hot cracking [9], and grain refinement in Ti alloys through Cu, Ni, and Ta additions [10, 11].

While in-situ alloying has significant potential, it also presents some important challenges, including the inhomogeneous distribution of powders, the evaporation of elements with low boiling points (which leads to changes in the chemical composition) and partial melting [12]. Blending, the pre-step of in-situ alloying has become much more important due to the need to ensure homogeneous distribution in the blends not only at macro but also micro level. Using powders with a smaller particle size for one element to satellite larger particles of other elements has the potential to solve this problem [8]. Significant differences in the thermal properties of the elements used can complicate parameter optimisation especially if elements with a high melting point such as Ta [13] are used, or changes in the chemical composition and evaporation if elements with a lower boiling point like Al and Mg are used [14].

Beyond structural applications, additive manufacturing has shown promise in functional materials such as soft magnetic alloys, which are vital in electrical and electromechanical devices. Soft magnetic alloys are defined by their low coercivity (typically below 1000 A/m), which relates to their ability to resist changes in magnetic orientation or, in other words, how easily their magnetic poles can be reversed. This soft magnetic behaviour is essential in a range of applications including electric motors, generators, transformers, magnetic shielding, etc., where soft magnetic alloys are used to offer a preferential path for magnetic flux [15].

Silicon steels tend to dominate the soft magnetic materials market having a balance of relatively high magnetic saturation, high relative permeability and low loss at an acceptable price point. Common grades such as those used in automotive traction motors have a silicon content of approximately 3%. Increasing the Si content causes a decrease in magnetic saturation (1.8–2.0 T to 1.6–1.7 T). However, it also increases electrical resistivity (reducing power loss as a result of limiting eddy current generation) and decreases magnetostriction (the property of magnetic materials which causes them to vibrate under alternating magnetisation and, in a coupled effect, change key magnetic properties when subjected to stress), which reaches near zero at 6.5% Si. These aspects are very important in many industrial applications [15–17].

According to the Fe–Si binary phase diagram, solidification begins in the disordered body-centered cubic (bcc) A2 phase and transforms into the B2 phase upon cooling. At lower temperatures, the remaining A2 and B2 phases further transform into B2 and $D0_3$ ordered phases [18, 19]. In the B2 phase, the presence of Si atoms at the centre of each bcc unit cell, and in the $D0_3$ phase, Si atoms occupying every third bcc cell centre, cause distortions in the slip planes, thereby increasing brittleness [20, 21]. Rapid solidification can suppress the formation of the $D0_3$ phase; however, suppression of the B2 phase is more complex and cannot be completely achieved [22]. High-silicon steels (> 3 wt% Si) offer superior magnetic properties, but are difficult to process via conventional techniques due to their brittleness which is caused by the formation of ordered intermetallic phases, specifically the B2 (FeSi) and $D0_3$ (Fe_3Si) ordered structures [23]. LPBF presents a compelling alternative, as it allows for the fabrication of complex geometries and brittle compositions that are otherwise unworkable.

Pioneering studies by Garibaldi et al. [24, 25] demonstrated the feasibility of producing Fe-6.9Si alloys via LPBF, establishing the foundation for exploring texture control and magnetic property optimization. Subsequent research has addressed the effects of processing parameters, heat treatment, and alloy composition on the microstructure and performance [26–28]. For example, Goll et al. [16] emphasized the importance of electrical insulation and topology-induced eddy current suppression in soft magnetic applications. Other studies have addressed the production of FeSi alloys across a range of compositions (2.4–10 wt% Si) and compared LPBF to DED, showing that LPBF typically yields finer grains and lower coercivity [29].

Despite these advances, defects such as porosity, cracks, and residual stresses remain critical challenges in the LPBF of soft magnetic materials. These defects stem from suboptimal energy densities—low densities cause lack-of-fusion pores, while high densities induce keyholing and cracking [17, 30]. Achieving dense, defect-free microstructures with desirable crystallographic texture requires precise control of a range of LPBF parameters, including laser power, scanning speed, and scanning strategy. Specifically, producing Goss or <001> textures—ideal for magnetic performance—necessitates conditions that promote columnar dendritic growth and keyhole melt pool morphology [31, 32].

Studies show that scanning strategy, energy input, and build direction influence texture development and magnetic performance [33–35]. Changing from a single scan to a double scan strategy on LPBF of the FeSi3 alloy, decrease hysteresis loss coefficient by around 0.02 J/kg [35]. Also a study on LPBF of FeSi6.9 shows that remanence values decrease from 0.8 to around 0.6 T and coercivity values decrease from 54 A/m to 50 A/m with increasing laser energy input up to 400 J/m [25]. Heat treatments further optimize magnetic properties by promoting grain growth, reducing dislocations, and eliminating Si micro-segregation [36, 37].

Application-driven research has validated the performance of LPBF-fabricated soft magnetic components. Transformer cores and electric motor components made

Table 1 Chemical composition provided by the supplier of the commercial powder used

Element	Fe	Si	C	S	O	*P*
Content, %	Balance	6.55	0.005	0.004	0.061	0.006

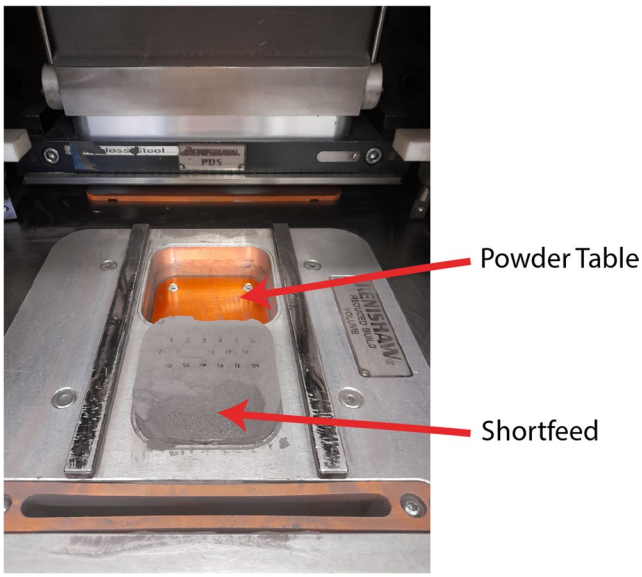

Fig. 1 Renishaw AM250 machine with reduced build volume kit, showing the short feed; photo taken before the samples produced with as blended powders were removed from the build table

from FeSi alloys have shown competitive performance with commercial non-oriented electrical M15 steel [34]. Notably, A stator core produced by FeSi6.5 material with LPBF method demonstrated 1.68 T magnetic saturation and 34.6 A/m coercivity, making it a strong candidate for high-efficiency motors and transformers [38].

The potential of in-situ alloying to simplify feedstock preparation and enable material innovation has not been explored in soft magnetic alloys. This study focuses on the in-situ alloying of FeSi6.5, a high-silicon soft magnetic alloy, using the LPBF technology. It aims to investigate the effects of in-situ alloying on the microstructure and magnetic properties in comparison with samples produced from commercial pre-alloyed powder. This investigation highlights the potential of in-situ alloying not only as a cost-effective alternative but also as a route to microstructural control and performance enhancement in soft magnetic materials fabricated by additive manufacturing.

2 Materials and methodology

Commercial FeSi6.5 powders (Fushel brand), with less than 0.1% impurity as shown in Table 1, were used as the base material. Elemental iron (Fe) and silicon (Si) powders, supplied by GoodFellow and Alfa Aesar respectively, were employed for in-situ alloying. The purities of Fe and Si powders were 99% and 99.5%, respectively.

A blended FeSi6.5 powder was prepared by mixing the elemental powders in a Turbula T2C mixer at 64 rpm for 2 h.

Particle size distribution measurements were conducted using a Malvern Mastersizer 3000. Phase analysis was performed via X-ray diffraction (XRD) using a PANalytical X'Pert Pro diffractometer with Ni-filtered Cu tube at an operating voltage of 40 kV and current of 40 mA.

The experimental samples were produced on a Renishaw AM-250 machine, using the reduced build volume (RBV) kit shown in Fig. 1, which uses a powder table system to provide the powder source. The machine is equipped with a pulsed ytterbium fibre laser ($\lambda = 1071$ nm), featuring a laser spot diameter of 75 µm. Unlike most LPBF systems that utilize continuous lasers, this setup employs a pulsed laser with a 10 µs delay between successive pulses. With the help of pre-trials, hatch distance was set to 75 µm, equal to the laser spot size. A stripe scanning strategy with a 67° rotation between layers was chosen [34]. The layer thickness was chosen as 30 µm, and laser power was set to 200 W. Figure 1 clearly shows the short feed typical for the experimental set-up employed for this experiment. A short feed is a build failure, where an insufficient amount of powder is deposited, resulting in reduced porosity and structural integrity of the samples produced. This is caused by the design of the powder table, which lets only a fixed amount of powder spread onto the build table.

Figure 2 shows the layout of the samples on the build plate, their dimensions and the scanning strategy employed. The process parameters employed were selected as follows: pulse point distances of 60 µm, 75 µm, and 90 µm, exposure times of 75 µs (~1 m/s scanning speed), 150 µs (~0.5 m/s), and 300 µs (~0.25 m/s) based on a 75 µm pulse point distance. An intermediate exposure time of 100 µs was also included to assess its potential suitability. Samples with 10 mm diameter and height were produced with the specified parameters. To mitigate the possible short feed effect, only the first two rows of samples were used, and others were reprinted again until all samples were acquired.

Samples produced using commercial pre-alloyed powder are marked as C, whereas those fabricated with as-blended powders are denoted as AB. For each parameter set, one sample was produced for each powder type and total 24 samples were produced.

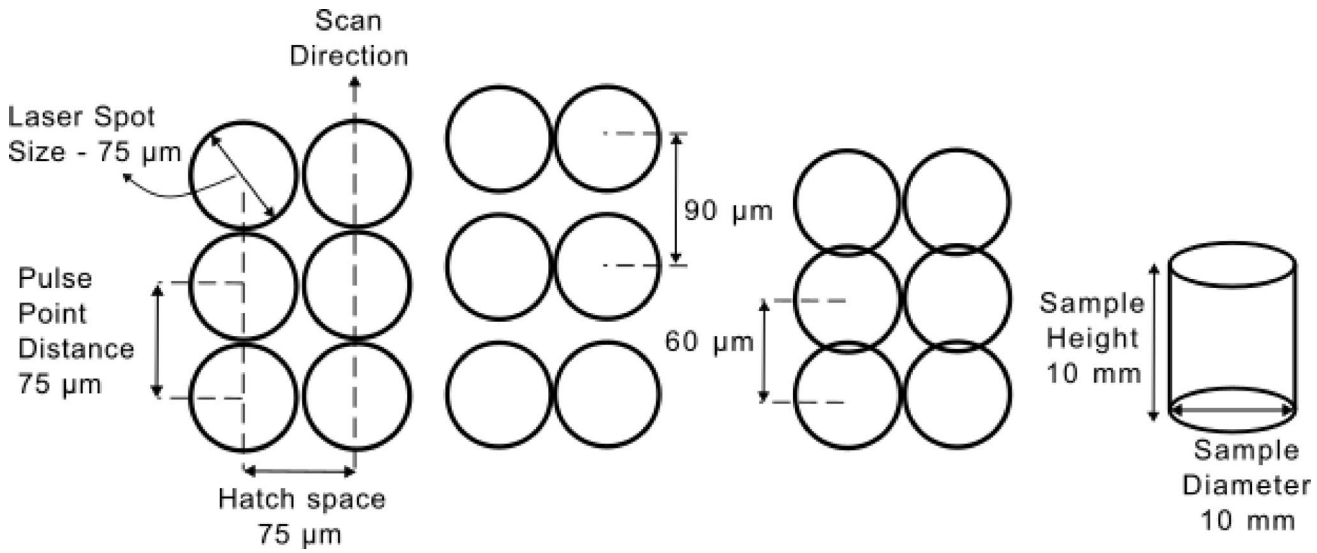

Fig. 2 Chosen laser scan parameters and sample dimensions

Table 2 Material properties of iron and silicon

	Iron	Silicon	References
Melting temperature (°C)	1538	1414	[42]
Thermal conductivity (W/m K)	80.4	149	[42]
Specific heat (J/kg°C)	450	710	[42]

Density measurements were conducted using the Archimedes' method. Isopropyl alcohol was used as a medium instead of pure water to minimize the effect of oxidation.

The samples were ground and polished, then etched with 2% NITAL solution. Microstructural characterization of the LPBF-fabricated samples was performed using a Leica optical microscope. Electron backscatter diffraction (EBSD) and energy-dispersive X-ray spectroscopy (EDS) analyses were performed using a Zeiss scanning electron microscope (SEM) equipped with a Nordlys detector from Oxford Instruments. EBSD scanning was conducted with a step size of 2 µm and a sample tilt angle of 70°. EBSD data were processed with the MTEX toolbox in MATLAB [39] to generate grain orientation maps and average grain size.

Magnetic characterization of the powders was conducted using a vibrating sample magnetometer (VSM) from Quantum Design. For bulk samples produced via LPBF, magnetic measurements were performed using a custom-built Direct Current (DC) magnetic characterization system [40].

To enable the comparison between commercial powder and in-situ alloying, this study uses a normalized, dimensionless volume energy density (E*) to provide a more universal indicator of the melting conditions than the traditional volumetric energy density (VED). Normalised energy density is a non-dimensional parameter that relates the laser processing parameters to material properties. The use of normalised energy density is suitable in the context of this study because it provides a material-independent, comparable measure of the energy input conditions for the two powders compared, which have different thermal properties.

The normalized -dimensionless – (E*) volume energy density was calculated by using the normalized laser power (P_n), layer thickness (l_n), hatch space (h_n) and scanning speed (v_n) values in the formula, respectively [41].

$$E^* = \frac{P_n}{l_n h_n v_n}, \text{ where}$$

$$P_n = \frac{AP}{r_b \lambda \Delta T}$$

A, P, r_b, λ, ΔT values are the surface absorptivity, laser power, beam radius, thermal conductivity and the difference between the melting temperature and the initial substrate temperature, respectively.

$$v_n = v r_b / \alpha$$

Scanning speed v is calculated by dividing the pulse point distance (d_p) value by the sum of the exposure time (t_e) and delay time (t_d). The thermal diffusivity α is calculated by dividing thermal conductivity to multiplication density and specific heat (c_p).

$$v = d_p / (t_e + t_d)$$

$$\alpha = \lambda / \rho c_p$$

Dimensionless hatch space h_n and layer thickness l_n are calculated using the following formulas, respectively.

$$h_n = h/r_b$$

$$l_n = l/(2r_b)$$

The mixture formula was used according to molar ratios (m_i) to calculate the characteristic properties (P_i) of the blended powder.

$$P_{ab} = P_{Fe} \times m_{Fe} + P_{Si} \times m_{Si}$$

The dimensionless energy density calculated in this study using values from [42], generally ranged from 2 to 16 which is consistent with findings reported in the literature [25, 27, 38, 43]. Despite the use of a relatively low dimensionless hatch spacing, certain samples achieved a relative density exceeding 90%. This observation is also in agreement with previous studies. As reported in [41], higher energy densities resulted in the formation of cracks, likely due to thermal stresses, while lower energy densities led to porosity caused by insufficient melting (see Fig. 3).

Finally, in accordance with previous studies, heat treatment was applied to improve the magnetic properties [17, 36]. Heat treatment was conducted in an argon atmosphere to prevent oxidation during the thermal process. The samples were heated at a controlled rate of 5 °C/min until reaching the target temperature of 1100 °C. Upon reaching this temperature, they were held isothermally for one hour to ensure uniform thermal exposure. Following the holding period, the furnace was turned off, and the samples were allowed to cool naturally to room temperature within the furnace.

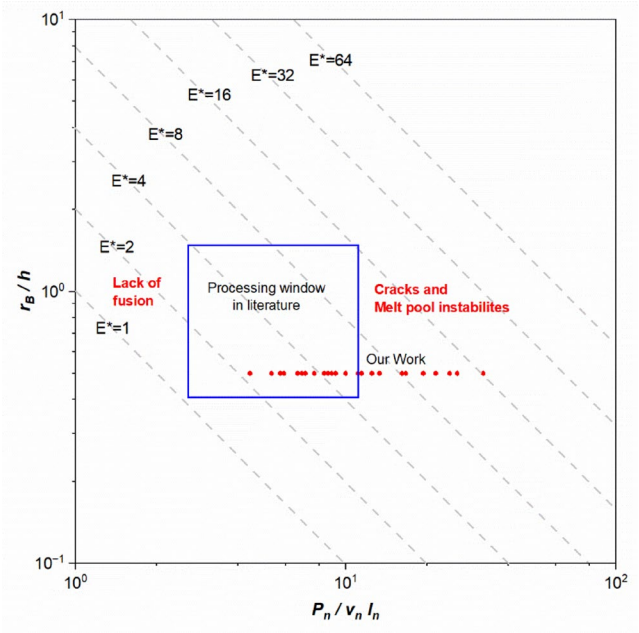

Fig. 3 Standardized process diagram of Fe-Si alloys based on Salazar et al. [41]

3 Results and discussion

3.1 Powders characterisation

Figure 4 shows the particle size distribution obtained from Mastersizer 3000, and the corresponding SEM images and XRD. Both the silicon and iron powders used during the study have irregular shapes. The measured Dv90 values for Fe, Si, as-blended and commercial powder are 65.7, 238, 51.5 and 61.5 µm respectively. The dimensional analysis showed experimental results of over 200 µm, while the company data of the commercial silicon powder is below 44 µm (325 mesh) due to the pure water used as solvent medium which was not able to disperse the agglomerated silicon particles. During the mixing process, iron particles broke down these large, agglomerated silicon powders because they were harder and acted like a milling ball. For this reason, no large particles were found in the as-blended powder analysis. Again, as a result of the mixing process, very small silicon powders adhered to the iron powders, as seen especially in the SEM image (Fig. 4). It is thought that this property increases homogeneity. Finally, in the XRD analysis, peaks specific to both iron and silicon are clearly seen in the as-blended alloy. This shows that although the iron particles behave like balls in mechanical alloying during blending, no mechanical alloying occurs. The commercial powder has the same peaks as the blended powder but without the small peaks of silicon powders which is expected because of the alloying. Also, it is important to note that the particles have spherical shapes which could have a potential impact on the LPBF process.

3.2 Evaluation of the LPBF process

As shown in Fig. 5, the relative density of the samples produced using commercial powder ranged narrowly between 94.2% and 97.7%, whereas those fabricated with the as-blended powders exhibited a broader range from 84.7% to 95.1%. Even though the chosen parameters are consistent with literature, the acquired relative densities are lower than expected. The short-feed effect seen in Fig. 1 was exacerbated with as blended powders' irregular morphology and low flowability, which hinder uniform powder distribution and result in localized regions with insufficient material for complete melting. The commercial powders' spherical morphology improves flowability, and the powders spread more uniformly, which results with higher relative densities.

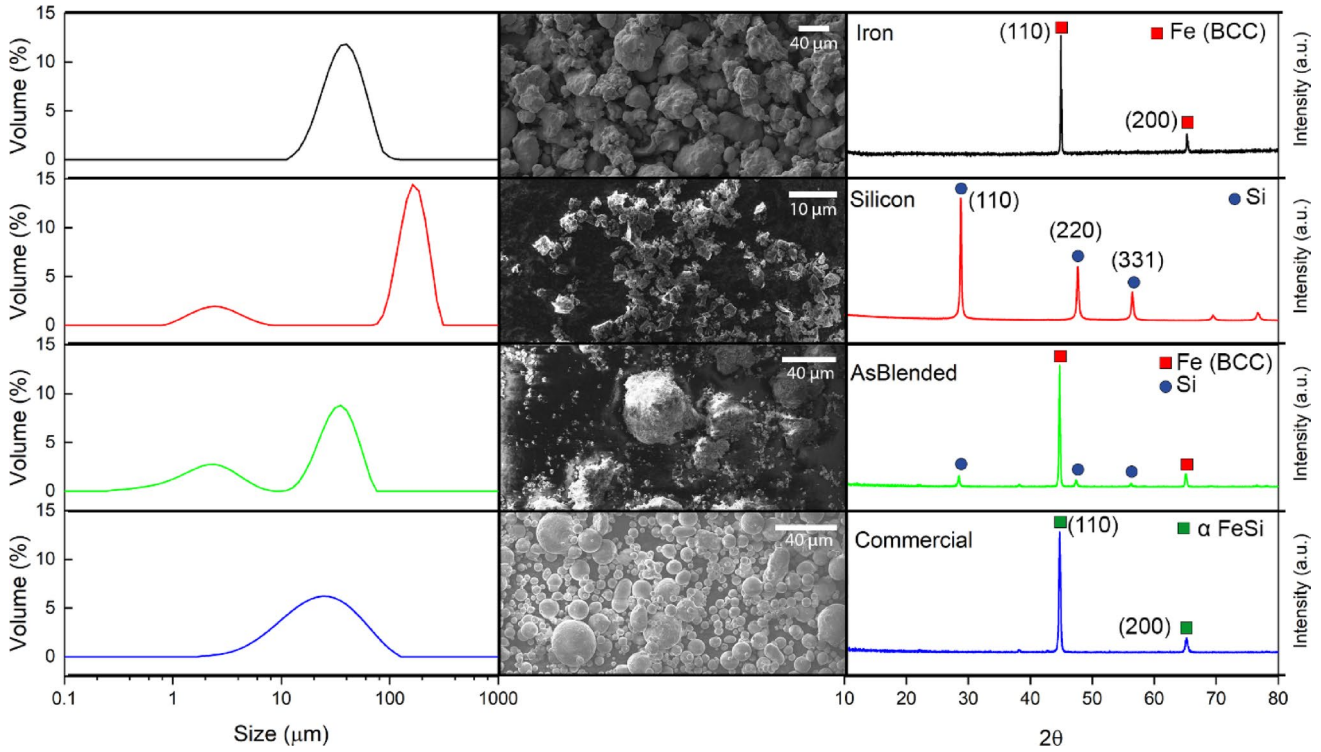

Fig. 4 Powder size analysis (left), SEM images (middle) and XRD pattern (right) of iron, silicon, as-blended and commercial FeSi6.5 powder

While the chosen parameter set improved relative densities, it was not enough to fully mitigate the effect of short feed.

Figure 6 shows the cross sections of etched samples obtained from optical microscope images. Microscopic examination revealed that, even at a lower energy input, the as-blended samples exhibited a keyhole-type melt pool morphology, while the commercial powder samples showed a conduction-type melt pool. This difference is attributed to the varying absorptivity of the powder types, with the as-blended powders likely absorbing more energy. The angular morphology of water-atomized powder particles results in a higher surface area-to-volume ratio, which enhances their capacity to absorb laser energy, potentially improving the sintering response [44].

In the commercial powder samples, lack-of-fusion type of porosity was only observed in the sample processed with the lowest energy density (75 µs–90 µm). In contrast, samples produced with as-blended powders had keyhole type porosity under the parameters which can be seen in Fig. 6.

Crack formation was observed in both powder types when processed with an exposure time of 300 µs, likely due to the high thermal stresses induced by excessive heat input [45].

Another notable observation is the presence of cracks in samples processed at 100 µs–75 µm. Although the cracks were finer in the commercial powder sample, they were present in both cases (Fig. 5). Furthermore, as shown in Fig. 6, an inter-layer crack extending through the layers is clearly visible in the sample produced with the 75 µs–75 µm parameters using commercial powder, leading us to conclude that the pulse point distance has a stronger influence on thermal stress than the exposure time.

3.2.1 Magnetic properties

Table 3 shows the magnetic properties of both commercial and as blended samples obtained from the hysteresis curves. The measured saturation magnetization values were found to be close to the theoretical value of 1.8 T for the FeSi6.5 alloy [46]. Overall, samples processed with a 90 µm pulse point distance tended to exhibit higher saturation magnetization values; however, no consistent or statistically significant correlation was established. With respect to exposure time, a slight increase in magnetization was observed in the 60 µm and 90 µm pulse point distance samples as exposure time increased, followed by a subsequent decline. One expected effect is that a higher relative density will give higher saturation magnetisation. However, in samples produced with commercial powders, a 3% change in relative density did not give correlated results with saturation magnetisation. Also, in samples produced with as blended powders, while lower relative densities caused lower saturation magnetisation, the effect was more limited than expected. Also, different samples with very similar relative

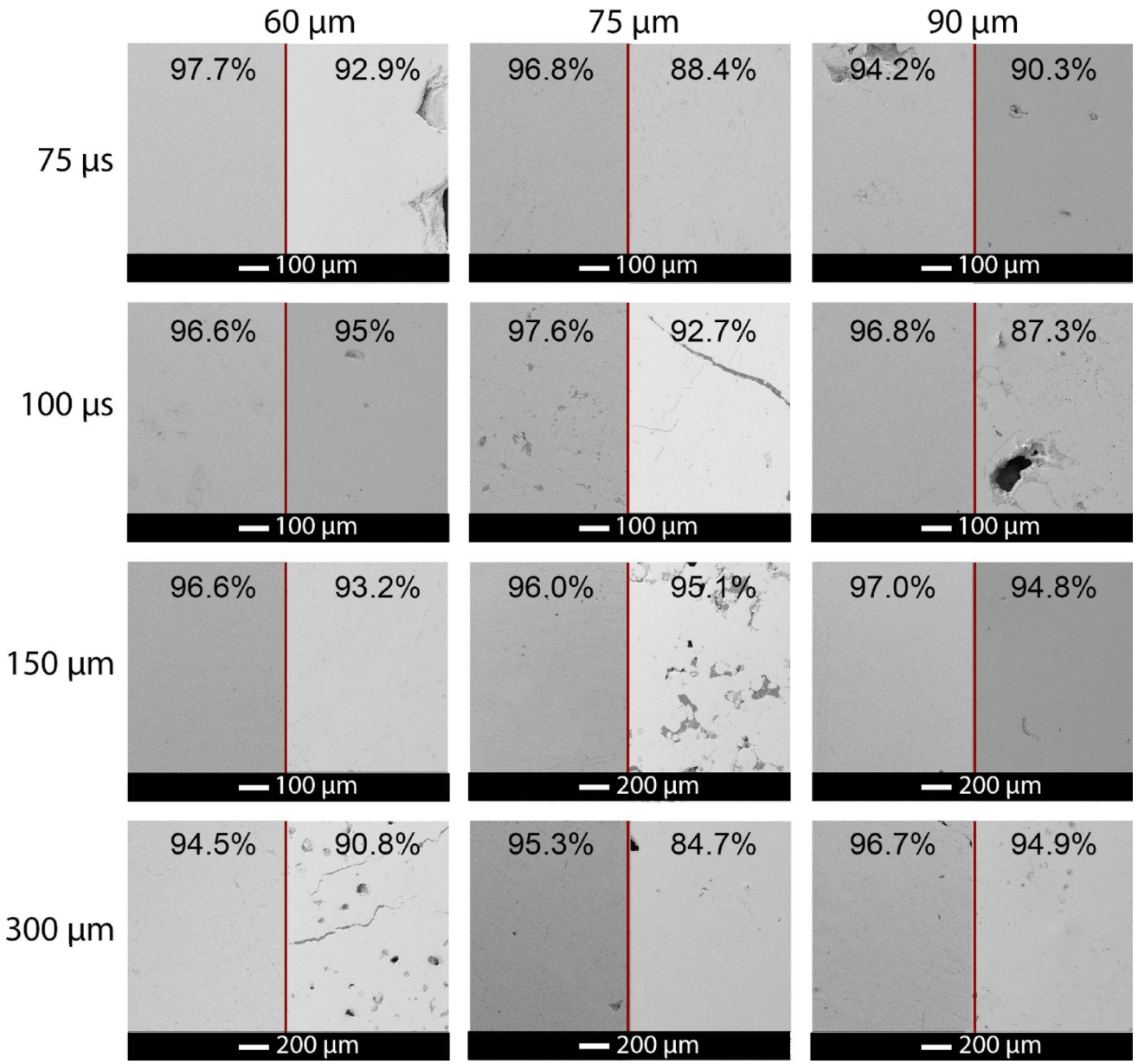

Fig. 5 SEM images (top view) and relative densities of samples manufactured using commercial power (left image) and as-blended powder (right image), using different pulse point distance and exposure time

densities had different values of coercivity, which cannot be explained by porosity. So, these variations in magnetic performance cannot be attributed only to porosity but are also affected by factors such as residual stress and grain size. Grain size and thermal stress have an effect on magnetic performance. Several studies on FeSi alloys show that heat treatment, which causes stress relief and grain growth, leads to improved magnetic performance and a decrease in coercivity [33, 47]. Samples produced with a different parameter set have different thermal process histories, which lead to different residual stresses. Even if they have the same relative density this will lead them to have different coercivities which is expected. This also helps to explain the comparatively lower magnetic performance of samples produced with a 75 µm pulse point distance.

An additional notable observation is that the influence of exposure time was less pronounced in samples produced with a 60 µm pulse point distance, whereas those fabricated with larger pulse point distances were more sensitive to exposure time variations. This behaviour is likely due to partial remelting effects.

In the case of as-blended powder samples, although the overall densities were lower than those of the commercial powder samples, the saturation magnetization values were

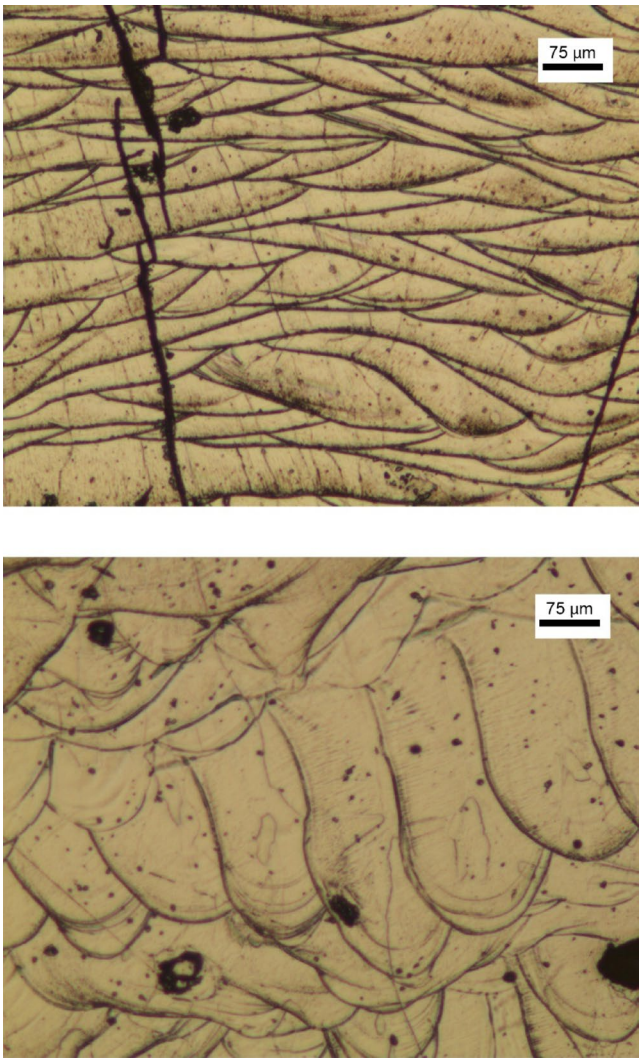

Fig. 6 Microscope image of etched cross-section of a commercial powder used sample produced with 75 µm pulse point distance − 75 µs exposure time (top) and as-blended powder used sample with of 75 µm pulse point distance of 75 µm–75 µs exposure time

generally comparable. A key point is that the magnetization values in the as-blended samples spanned a broader range. The influence of pulse point distance on magnetic performance varied with exposure time, but, consistent with the commercial samples, those produced with a 75 µm pulse point distance generally demonstrated lower saturation magnetization.

The measured coercivity values at zero point for both commercial and as-blended samples were in the range 761.3–1755.9 A/m, higher than those typically expected for soft magnetic materials (< 1000 A/m) [48]. This increase is attributed primarily to the relatively fine grain structures and the presence of residual thermal stresses. In general, the as-blended samples generally exhibited lower coercivity (784.9–1357.6 A/m) compared to the commercial samples (761.3–1755.9 A/m). This difference is likely to be due to the coarser grain structure observed in the as-blended samples.

For the samples produced using commercial powder, remanence values range from 0.04 to 0.21 T. In contrast, the samples produced using as-blended powder show a narrower remanence range of 0.08–0.15 T, exhibiting less sensitivity to processing parameters. The relatively stable remanence across different energy densities in AB samples indicate that lower coercivity values promote a more uniform magnetic response, even though overall magnetisation remains slightly lower due to residual porosity and microstructural inhomogeneities.

3.3 Evaluation of microstructure and phases

Figure 6 clearly shows the columnar grains extending across multiple layers in the samples. In the as-blended powder specimen, smaller equiaxed grains are also observed at the centre of the melt pool; nevertheless, EBSD analysis using Matlab-based grain size quantification reveals that the commercial sample exhibits an overall coarser grain structure

Table 3 Magnetic properties of commercial (C) and as-blended (AB) samples

Pulse point distance (µm)	Exposure time (µs)	Coercivity (A/m)		Saturation magnetisation (T)		Remanence (T)	
		C Samples	AB Samples	C Samples	AB Samples	C Samples	AB Samples
60	75	1287.3	916.3	1.67	1.38	0.10	0.13
60	100	1556.4	1018.4	1.69	1.39	0.21	0.08
60	150	1502.9	1355.4	1.65	1.72	0.20	0.14
60	300	1755.9	871.6	1.33	1.57	0.04	0.15
75	75	1213.8	921.5	1.67	1.55	0.13	0.15
75	100	1126.3	868.8	1.50	1.58	0.08	0.08
75	150	1120.0	784.9	1.65	1.28	0.08	0.11
75	300	761.3	1192.7	1.48	1.47	0.06	0.13
90	75	812.3	1162.3	1.52	1.67	0.04	0.13
90	100	1111.2	1020.3	1.88	1.47	0.17	0.11
90	150	1271.9	952.7	1.71	1.72	0.14	0.13
90	300	1049.0	1357.6	1.63	1.71	0.11	0.10

under the same parameter conditions. Even though we believe a higher absorbed energy during LPBF processing of the as-blended powder will increase grain coarsening through an extended melt-pool lifetime and slower solidification rates, the higher presence of impurities acts as nucleation sites in the melt pool and causes more grain formation in total.

One of the primary challenges in in-situ alloying is compositional inhomogeneity. In this context, the EDS images presented in Fig. 7 clearly show homogeneous Si distribution in the as-blended sample. The absence of any observable segregation is attributed to both effective mixing and the adherence of fine Si particles to Fe particles, resulting in a uniform distribution. Furthermore, it is considered that the melt pool conditions were sufficient to ensure complete mixing of liquid Fe and Si during processing. Although the interaction time may appear short, it is believed that the forces acting within the melt pool are adequate to facilitate the required mixing efficiency.

Figure 8 displays the EBSD results obtained from cross-sections of samples produced with commercial and as-blended powders. To improve comparability, we examined samples that were produced using the same parameters, exhibited high relative density, and showed the same saturation magnetisation. The as-blended sample shows a smaller grain size in the evaluated area compared to the commercial sample. In terms of texture, the as-blended sample exhibits a higher degree of texture, with the (001) planes mainly oriented in the building direction (BD), while the commercial sample shows a lower preferential orientation. According to Cong, in BCC samples, the magnetic properties are maximized when the grains are oriented in the [001] direction [49]. This implies that a single grain evaluated magnetically in the [001] direction should reach magnetic saturation more quickly than in other directions. In this study, the as-blended sample shows lower coercivity than the commercial sample (see Table 1, samples fabricated with 90 µm – 150 µs parameters). Although the grain size in the commercial sample is larger than in the as-blended sample—an aspect that would typically favour lower coercivity in the commercial sample—the higher degree of grain orientation observed in the as-blended sample may have had a stronger influence on coercivity.

The XRD scans in Fig. 8e, f show that the only acquired phase is α-FeSi for both powder types. At around 20°, there is a broad peak, which can come from oxides and/or other phases. However, for these a suitable match couldn't be found in the Crystallography Open Database. Also, in Fig. 8e, there are several smaller peaks with a partial match to the DO3 phase which requires higher Si content (at.%Si > 12). While this is possible, since the as-blended powder can have micro inhomogeneities with higher Si content, this still needs further investigation.

3.4 Results of heat treatment

Following the heat treatment applied to the selected samples, a significant reduction in coercivity was observed across all specimens (Fig. 7). Notably, coercivity decreased by up to an order of magnitude—approximately 10-fold in the commercial samples and up to 8-fold in the as-blended samples. Both residual stresses and grain boundaries act as effective pinning sites that impede magnetic domain wall motion [50]. With heat treatment, the residual stresses introduced during the LPBF process are largely relieved and grain coarsening occurs, thereby facilitating domain wall movement and decreasing coercivity. As all coercivity values dropped below 1000 A/m, the samples can be classified as exhibiting soft magnetic behaviour.

Post heat treatment, the variation in coercivity among samples with different exposure times was notably reduced, indicating a homogenizing effect on magnetic properties.

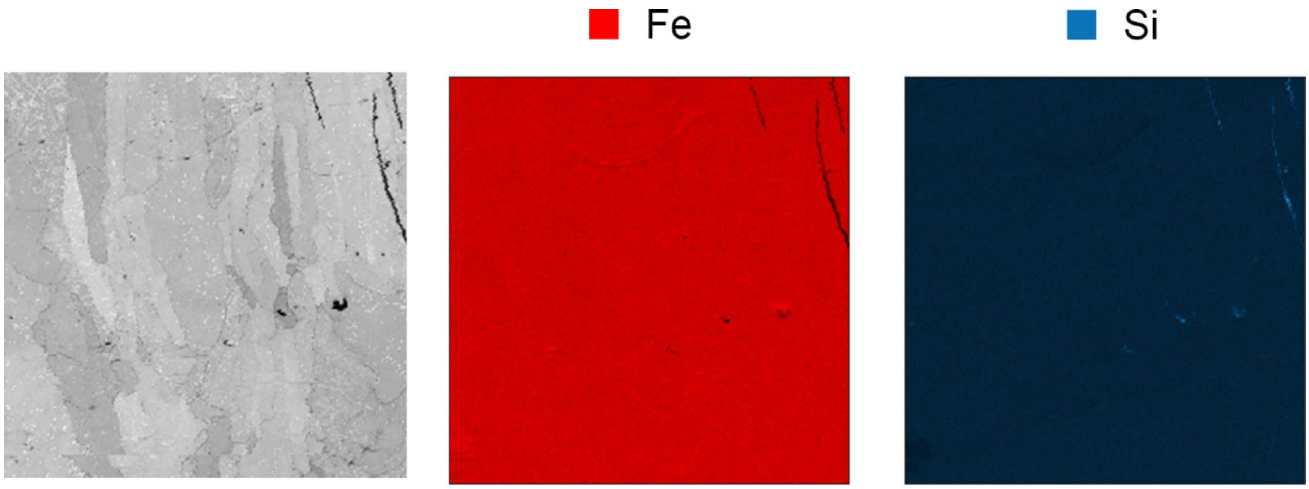

Fig. 7 EDS images of as-blended powder used samples produced with pulse point distance of 90 µm and exposure time of 150 µs

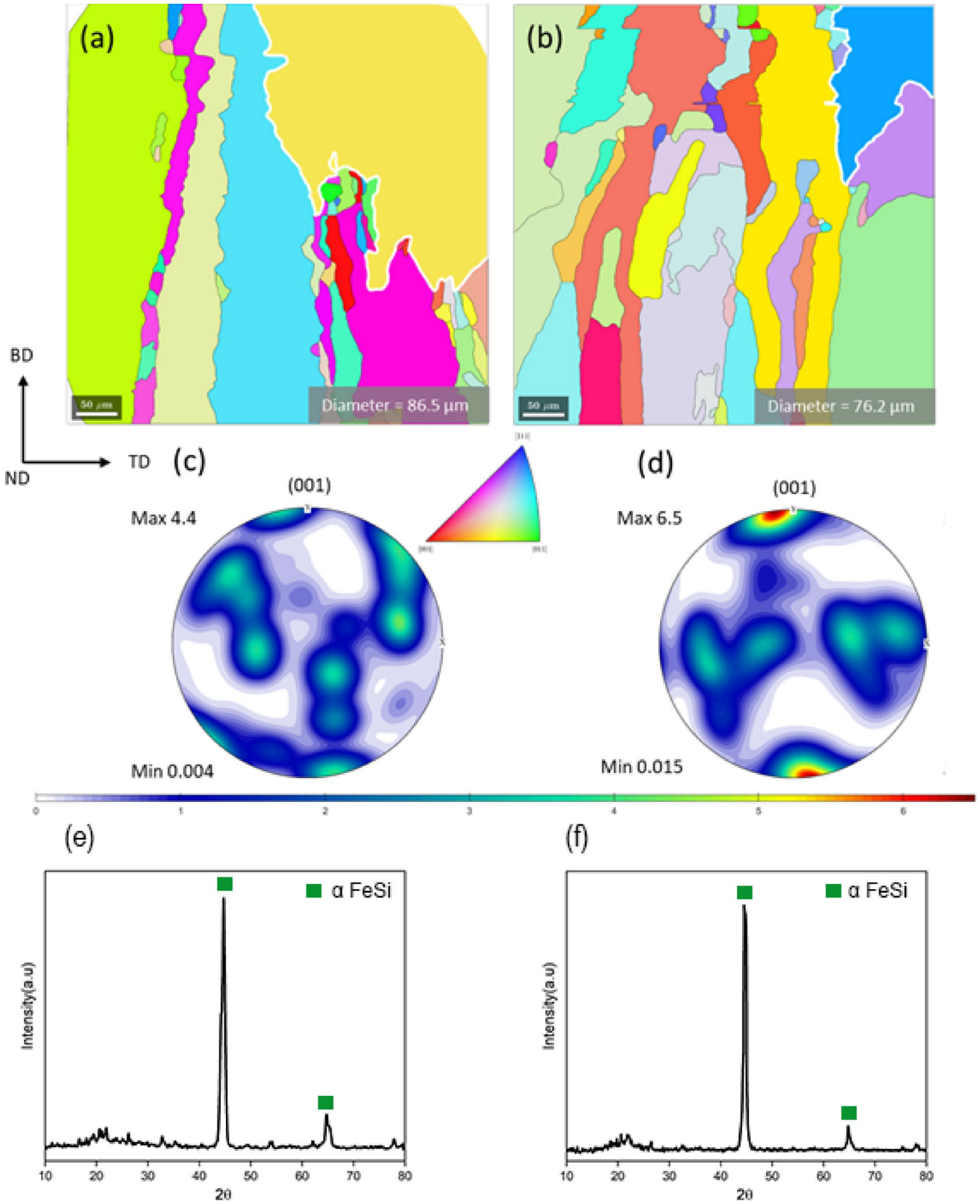

Fig. 8 EBSD result obtained from the cross-section of samples produced with 90 µm–150 µs parameters (**a**) commercial, (**b**) as-blended sample. IPF map and the polar figure for the (001) plane for (**c**) commercial, (**d**) as-blended sample. XRD patterns of the samples produced with 90 µm–150 µs parameters (**e**) commercial, (**f**) as-blended sample

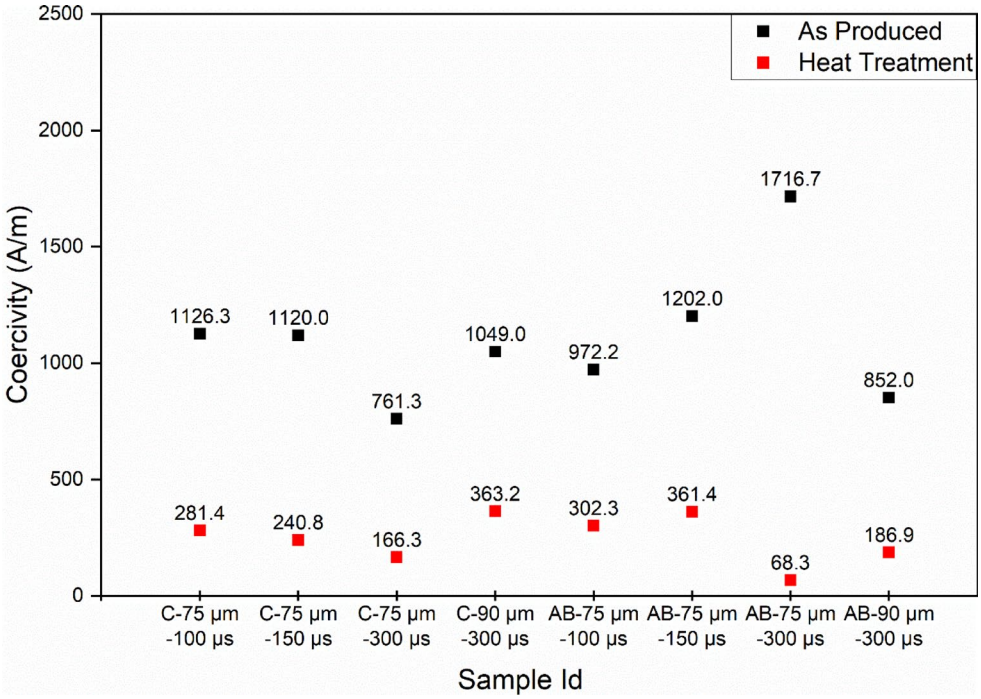

Fig. 9 Comparison of coercivity values of as produced and heat-treated samples, (C in sample id indicates commercial powder and AB is used for as-blended powder)

However, samples produced with higher pulse point distances retained relatively higher coercivity values in both powder types. This can be attributed to differences in grain growth behaviour: in samples with lower pulse point distances, the grains at intersection regions already possessed excess energy due to overlapping melt tracks. This pre-existing energy likely accelerated grain growth during heat treatment, thereby reducing coercivity more effectively in these samples. Figure 9 showed a keyhole melt type while commercial sample had a conduction type for same parameters, which is an indirect indication of as-blended samples absorbed more energy in LPBF process. Because the as-blended samples have more pre-existing energy in same process conditions, the reduction in coercivity following heat treatment was more significant in the as-blended samples.

4 Conclusion

In this study, the in-situ alloying approach was successfully integrated into the Laser Powder Bed Fusion (LPBF) process to fabricate FeSi6.5 soft magnetic material.

Among the as-blended samples, the most optimal magnetic and microstructural properties were achieved using the processing parameters of 90 µm pulse point distance and 150 µs exposure time. For the commercial powder samples, the most favourable results were obtained with the parameters 90 µm–100 µs.

The as-blended samples exhibited lower relative density values, primarily due to poor flowability resulting from the irregular shape of the powder particles. However, the satellite distribution of the Si powder contributed positively to the compositional homogeneity, and no evidence of segregation was observed. In both types of samples, it was not possible to achieve relative density above 99% due to the micro voids caused by the short feed of the powder feed system.

The melt pool morphology differed significantly between the two powder types, driven by variations in absorptivity. The as-blended samples tended to form keyhole-type melt pools, whereas conduction-mode melt pools were observed in the commercial powder samples.

The magnetic properties in the samples using as-blended powder were distributed within a narrower range (1.28–1.72 T B_s, 784–1357 A/m, 0.08–0.15 T B_r), while a broader variation was observed in the samples using commercial powder (1.33–1.88 T B_s, 761–1755 A/m, 0.04–0.21 T B_r). In terms of magnetic performance, the as-blended samples exhibited superior coercivity and relative permeability values, whereas the commercial samples demonstrated higher saturation magnetization. These differences are attributed to the coarser grain structure in the as-blended samples and the lower impurity content in the commercial powder.

The heat treatment led to grain growth and decrease in the coercivity of all samples produced using both commercial and as-blended powders. The extent of its effect on the microstructure varied depending on the pulse point distance parameters.

Acknowledgements The authors would like to express their sincere gratitude to Prof. M. Lütfi Öveçoğlu for granting access to the Powder Materials Laboratories at Istanbul Technical University (ITU) for powder preparation, Dr. Julian Steer for access Malvern Mastersizer 3000 for powder characterisation and to Prof. Sam Evans for providing access to the characterisation laboratory. This study was supported by the Ministry of National Education of the Republic of Türkiye.

Author contributions Mümin Biyiklioglu: Writing—original draft, methodology, investigation, conceptualization, data curation. Carolina Guerra Figueroa: Writing—original draft, Investigation, data curation. Rossitza Setchi: Writing—review and editing, methodology, conceptualization, supervision. Philip Anderson: Writing—review and editing, supervision.

Data availability No datasets were generated or analysed during the current study.

Declarations

Conflict of interest The authors declare no competing interests.

References

1. Gu D et al (2021) Material-structure-performance integrated laser-metal additive manufacturing. Science 372(6545):eabg1487
2. Volpato GM, Tetzlaff U, Fredel MC (2022) A comprehensive literature review on laser powder bed fusion of inconel superalloys. Additive Manuf 55:102871
3. Jandaghi MR et al (2022) In-situ alloying of stainless steel 316L by co-inoculation of Ti and Mn using LPBF additive manufacturing: microstructural evolution and mechanical properties. Mater Sci Eng A 857:144114
4. Dejene ND, Lemu HG (2023) Current status and challenges of powder bed fusion-based metal additive manufacturing: literature review. Metals 13(2):424
5. Jandaghi MR et al (2022) In situ alloying of AlSi10Mg-5 wt% Ni through laser powder bed fusion and subsequent heat treatment. J Alloys Compd, 904
6. Kang N et al (2017) Microstructure and strength analysis of eutectic Al-Si alloy in-situ manufactured using selective laser melting from elemental powder mixture. J Alloys Compd 691:316–322
7. Kang N et al (2016) Wear behavior and microstructure of hypereutectic Al-Si alloys prepared by selective laser melting. Appl Surf Sci 378:142–149
8. Simonelli M et al (2018) A comparison of Ti-6Al-4V in-situ alloying in selective laser melting using simply-mixed and satellited powder blend feedstocks. Mater Charact 143:118–126
9. Montero-Sistiaga ML et al (2016) Changing the alloy composition of Al7075 for better processability by selective laser melting. J Mater Process Technol 238:437–445
10. Zhang D et al (2019) Additive manufacturing of ultrafine-grained high-strength titanium alloys. Nature 576(7785):91–95
11. Barriobero-Vila P et al (2018) Peritectic titanium alloys for 3D printing. Nat Commun 9(1):3426
12. Jandaghi MR et al (2022) In situ alloying of AlSi10Mg-5 wt% Ni through laser powder bed fusion and subsequent heat treatment. J Alloys Compd 904:164081
13. Huang S et al (2020) Laser powder bed fusion of titanium-tantalum alloys: compositions and designs for biomedical applications. J Mech Behav Biomed Mater 108:103775
14. Shoji Aota L et al (2020) Laser powder-bed fusion as an alloy development tool: parameter selection for in-situ alloying using elemental powders. Materials 13(18):3922
15. Ouyang G et al (2019) Review of Fe-6.5 wt%Si high silicon steel: a promising soft magnetic material for sub-kHz application. J Magn Magn Mater 481:234–250
16. Macknojia AZ et al (2024) Additive manufacturing of Fe-6.5 wt.% Si transformer steel toroidal cores: process optimization, design aspects, and performance. Mater Design 241:112883
17. Stornelli G et al (2021) Properties of additively manufactured electric steel powder cores with increased Si content. Materials 14(6):1489
18. Shin J et al (2005) Ordering–disordering phenomena and microhardness characteristics of B2 phase in Fe–(5–6.5%) Si alloys. Mater Sci Engineering: A 407(1–2):282–290
19. Wittig J, Frommeyer G (2008) Deformation and fracture behavior of rapidly solidified and annealed iron-silicon alloys. Metall Mater Trans A 39(2):252–265
20. Lemke J et al (2017) Calorimetric study and microstructure analysis of the order-disorder phase transformation in silicon steel built by SLM. J Alloys Compd 722:293–301
21. Viala B et al (1996) Study of the brittle behaviour of annealed Fe-6.5 wt% Si ribbons produced by planar flow casting. Mater Sci Eng A 212(1):62–68
22. Wang X et al (2015) Effect of cooling rate on order degree of 6.5 wt.% Si electrical steel after annealing treatment. IEEE Trans Magn 51(11):1–4
23. Backes C et al (2024) Microstructure and magnetic domain structure of additively manufactured Fe–Si soft magnetic alloys with 3 and 9 wt.-% Si. J Mater Res Technol 29:1691–1702
24. Garibaldi M et al (2016) Metallurgy of high-silicon steel parts produced using selective laser melting. Acta Mater 110:207–216
25. Garibaldi M et al (2018) Relationship between laser energy input, microstructures and magnetic properties of selective laser melted Fe-6.9% Wt Si soft magnets. Mater Charact 143:144–151
26. Hwang JY, Jung HY (2024) Fabrication of Fe-6.7 wt% Si steel via laser powder bed fusion and investigation of the resulting crystallographic texture. Progress Additive Manuf. 1–10
27. Goll D et al (2019) Additive manufacturing of soft magnetic materials and components. Additive Manuf 27:428–439
28. Andreiev A et al (2023) Powder bed fusion of soft-magnetic iron-based alloys with high silicon content. J Mater Process Technol 317:117991
29. Varahabhatla SM et al (2023) Influence of energy density on the microstructure, growth orientation, and anisotropy of magnetic properties in additively manufactured Fe-3.8 wt% Si transformer steels. Materialia 30:101854
30. Yakout M et al (2019) Selective laser melting of soft magnetic alloys for automotive applications. in Joint Special Interest Group meeting between euspen and ASPE
31. Lee H et al (2024) Effect of process parameters on the texture evolution of Fe-6.5 wt% Si soft magnetic alloys manufactured via laser powder bed fusion. J Mater Process Technol 331:118521

32. Trapp J et al (2017) In situ absorptivity measurements of metallic powders during laser powder-bed fusion additive manufacturing. Appl Mater Today 9:341–349
33. Haines M et al (2022) Role of scan strategies and heat treatment on grain structure evolution in Fe-Si soft magnetic alloys made by laser-powder bed fusion. Addit Manuf 50:102578
34. Plotkowski A et al (2020) Design and performance of an additively manufactured high-Si transformer core. Mater Design 194:108894
35. Plotkowski A et al (2019) Influence of scan pattern and geometry on the microstructure and soft-magnetic performance of additively manufactured Fe-Si. Addit Manuf 29:100781
36. Garibaldi M et al (2018) Effect of annealing on the microstructure and magnetic properties of soft magnetic Fe-Si produced via laser additive manufacturing. Scr Mater 142:121–125
37. Jiang L et al (2024) Influence of annealing treatment on grain growth, texture and magnetic properties of a selective laser melted Fe-6.5 wt% Si alloy. J Mater Res Technol 32:1324–1341
38. Koo B et al (2021) Structurally-layered soft magnetic Fe-Si components with surface insulation prepared by shell-shaping selective laser melting. Appl Surf Sci 553:149510
39. Bachmann F, Hielscher R, Schaeben H (2010) Texture analysis with MTEX–free and open source software toolbox. Solid State Phenom 160:63–68
40. Anderson P (2008) A universal DC characterisation system for hard and soft magnetic materials. J Magn Magn Mater 320(20):e589–e593
41. Salazar AAV et al (2024) A Normalized diagram for compare densities in additive manufacturing of iron-silicon magnetic alloys. In: Technological Systems, sustainability and safety
42. Desai PD (1986) Thermodynamic properties of iron and silicon. J Phys Chem Ref Data 15(3):967–983
43. Zaied M et al (2022) Additive manufacturing of soft ferromagnetic Fe 6.5% Si annular cores: process parameters, microstructure, and magnetic properties. IEEE Trans Magn 58(11):1–9
44. Averardi A et al (2020) Effect of particle size distribution on the packing of powder beds: a critical discussion relevant to additive manufacturing. Mater Today Commun 24:100964
45. Yao S et al (2023) LPBF-Formed 2024Al alloys: process, microstructure, properties, and thermal cracking behavior. Metals 13(2):268
46. Tumanski S (2016) Handbook of magnetic measurements. CRC
47. Gao S et al (2023) Effects of heat treatment on the microstructures and magnetic properties of selective laser melted Fe-3 wt% Si functional soft magnet. J Alloys Compd 951:169840
48. Commission IE (2016) IEC 60404-1, in Magnetic materials: part 1: classification
49. Cong J et al (2021) Optimum magnetic properties of non-oriented electrical steel produced by compact strip production process. Metals 12(1):64
50. Liogas KA et al (2023) Effect of heat treatment on the microstructure and magnetic properties of laser powder bed fusion processed equiatomic Co-Fe. Additive Manuf 67:103499